High Step-Up PV Module Integrated Converter for PV Energy Harvest in FREEDM Systems

António Manuel Santos Spencer Andrade, *Student Member, IEEE*, Luciano Schuch, *Member, IEEE*, and Mario Lúcio da Silva Martins, *Member, IEEE*

***Abstract*—This paper proposes a novel single-switch dc/dc converter for the future renewable electric energy delivery and management system to implement the distributed renewable energy resources (DRER). The DRER is responsible for the maximum power point tracking of the photovoltaic panel (PV) module and also for the control of central energy storage device. Due to the characteristics of the PV module and the dc-bus, the single power stage must provide low current ripple in the input and output terminals, must operate with output current and voltage regulation, and present a high-voltage conversion ratio. To achieve such features, this paper proposes a novel integrated Boost–Zeta converter. To avoid a complex modeling and control, we propose a disaggregation concept for this. Experimental results are presented for the purpose of operating the converter and also for the operation of the system.**

***Index Terms*—DC/DC converter, DC microgrid, high step-up, microgrid.**

I. Introduction

THE interest in distributed and renewable energy resources has continuously increased over the last few years. The distribution grid delivery and management system have become a concern in an interesting research area [1]–[5]. The extensive employment of renewable energy depends on an advanced smart grid infrastructure where the users have the ability to manage their energy consumption as well as use plug-and-generate and plug-and-store energy devices at home and in industrial applications [6]–[8].

Proposed by Huang [9], the future renewable electric energy delivery and management (FREEDM) is an intelligent electric power grid integrating highly distributed and scalable alternative generating sources and storage with existing power systems to facilitate a renewable energy-based society [10]–[12].

The FREEDM system consists of two different devices: the distributed renewable energy resource (DRER), dedicated to harvest the maximum power point (MPP) from the renewable energy resource; and the distributed energy storage device (DESD), dedicated to control the charging/discharging process of the central energy storage devices (CESD) [13]–[16]. Each of them operates separately. Nevertheless, differently than the MPP approach, the use of distributed storage devices would not be efficient as the dc/dc interface of the DESD losses would reduce the system efficiency. Hence, an alternative approach consists of making use of an external CESD (battery stack) connected directly to the dc-bus of the photovoltaic panel (PV) module integrated system. It means that the dc/dc converters in the proposed system present both functions, i.e., they harvest the maximum power from the renewable energy resource and control the charging/discharging process of a DESD, as shown in Fig. 1(b). It can be seen that the proposed system makes use of a single battery stack that is connected to the dc-bus as a CESD. The battery stack charging is shared by all PV module integrated systems that are connected to the dc-bus [see Fig. 1(b)]. Meanwhile, all DRER converters operate in the same way. According to the battery pack current and voltage values, the DRER converter operates in three modes: maximum power point tracking (MPPT) mode, constant-current (CC) mode, and constant-voltage (CV) mode.

The most common battery charging methods presented in the literature are the method of CC, the method of CV [17], and the combination of both—the CC/CV method [18]. As the name suggests, this method consists of two stages of charge which are named CC stage and CV stage. During the CC stage, a CC level is imposed to the battery. This controlled current is applied to the battery until its voltage reaches the float voltage level (V_{flut}). Since the current value applied during the CC stage only controls the charging rate, this value can vary within a range which is limited between zero and by the maximum charge current allowed by the battery without damaging its parts. This way, in the PV battery charger proposed, the MPPT current defines the current level during the CC stage. Hence, as long as the charging current level is lower than the maximum charging current, the MPPT algorithm controls the converter.

The main objective of this paper is to propose a new converter that fits the characteristics of the proposed modified FREEDM system [see Fig. 1(b)], with the aim to explain the steady-state operation and the dynamic operation, to present control, to illustrate design, and to demonstrate experimental results of the proposed converter. The paper is outlined as follows. The DRER converter is explained in Section II. The principle of

Manuscript received June 18, 2016; revised August 22, 2016; accepted October 17, 2016. Date of publication October 25, 2016; date of current version March 17, 2017. Paper 2016-IPCC-0142.R1, presented at the 2015 IEEE Energy Conversion Congress and Exposition, Montreal, QC, Canada, Sep. 20–24, and approved for publication in the IEEE Transactions on Industry Applications by the Industrial Power Converter Committee of the IEEE Industry Applications Society. This work was supported by the National Council of Technological and Scientific Development–CNPQ (481612/2012-2 and 309748/2012-7).

The authors are with the Federal University of Santa Maria, Santa Maria 97105-900, Brazil (e-mail: antoniom.spencer@gmail.com; profschuch@gmail.com; mariolsm@gmail.com).

Digital Object Identifier 10.1109/TIA.2016.2621110

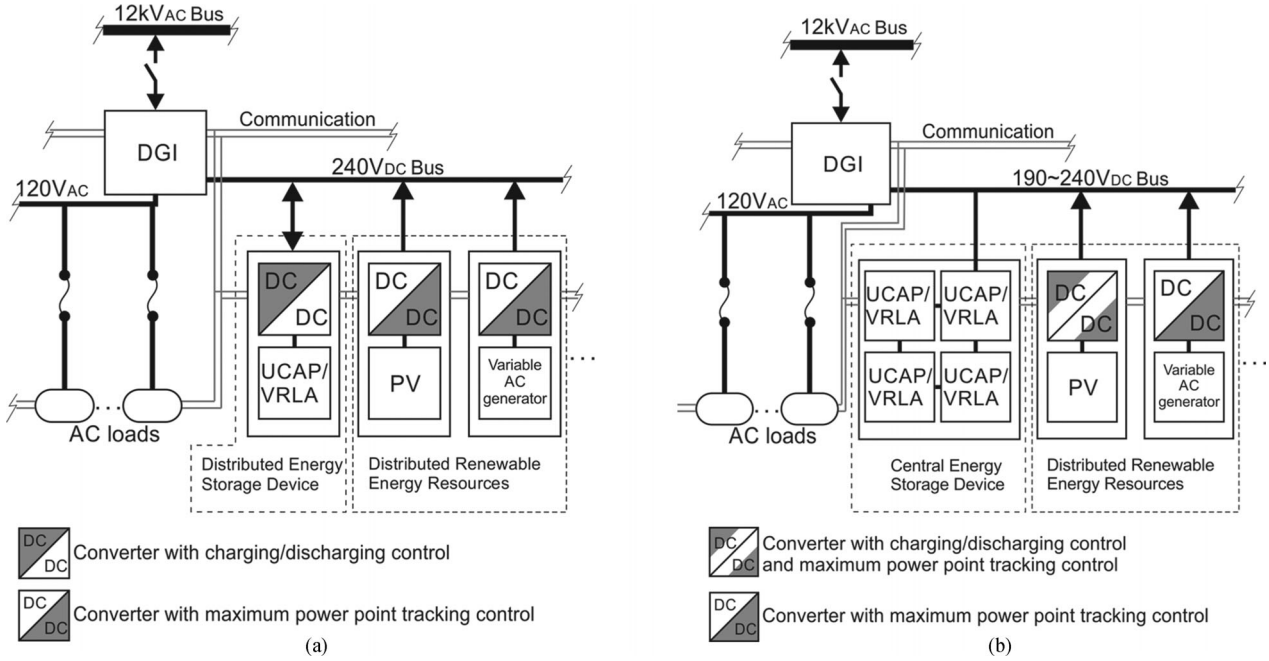

Fig. 1. Diagram of the systems: (a) FREEDM system; (b) proposed modified FREEDM system; and (c) power flow.

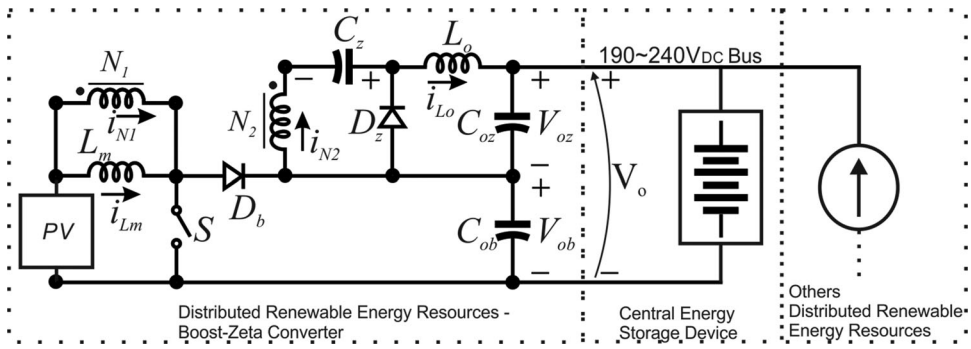

Fig. 2. Proposed integrated Boost–Zeta converter.

operation and the steady-state analysis of the proposed converter are illustrated in Sections III and IV, respectively. Then, a comparative analysis and the modeling and control are showed in Sections V and VI. Experimental results on a laboratory prototype of 250 W are demonstrated in Section VII. Finally, the conclusion is in Section VIII.

II. DRER DC/DC Converter

It should be noticed that due to their high series equivalent resistance standard single-switch single-ended converters (for instance boost and buck–boost topologies) cannot be used to implement the DRER converter since it demands very high duty cycles [19]–[21] to handle the voltage difference between a single PV module and the 240 V of the dc-bus. This high conversion ratio is achieved with a novel nonisolated high step-up dc–dc converter proposed in this paper. This dc–dc converter is based on the integration of the Boost and the Zeta converters.

The DRER converter (see Fig. 2) is comprised of a single-switch dc/dc converter with an input, middle section, and output section, where the input section consists of PV source, the switch, and primary of the coupled-inductor composed of L_m, N_1, and N_2. The middle section is given by secondary of the coupled inductor and the capacitor C_z. Finally, the output section can be split into two parts. The output section of the Boost converter is comprised of a diode D_b and the capacitor $C_{\rm ob}$, and the output section of the Zeta converter is given by diode D_z, inductor L_o, and the capacitor $C_{\rm oz}$, where their connection is in stacked $(V_{\rm ob} + V_{\rm oz})$. Note that in the output section is the inductor L_o, therefore the output current has low ripple and the possibility of controlling this current. The converter is named Boost–Zeta integrated converter.

III. Integrated Boost–Zeta Converter

Fig. 3 shows a circuit diagram of the proposed integrated Boost–Zeta converter. S is the power MOSFET and D_b and D_z are the diodes of the Boost and Zeta cells converters, respectively. L_m and N_1 are the primary coupled inductor, where L_m is the magnetizing inductance. N_2 is the secondary of the coupled inductor. C_z is the buffer capacitor of the Zeta converter.

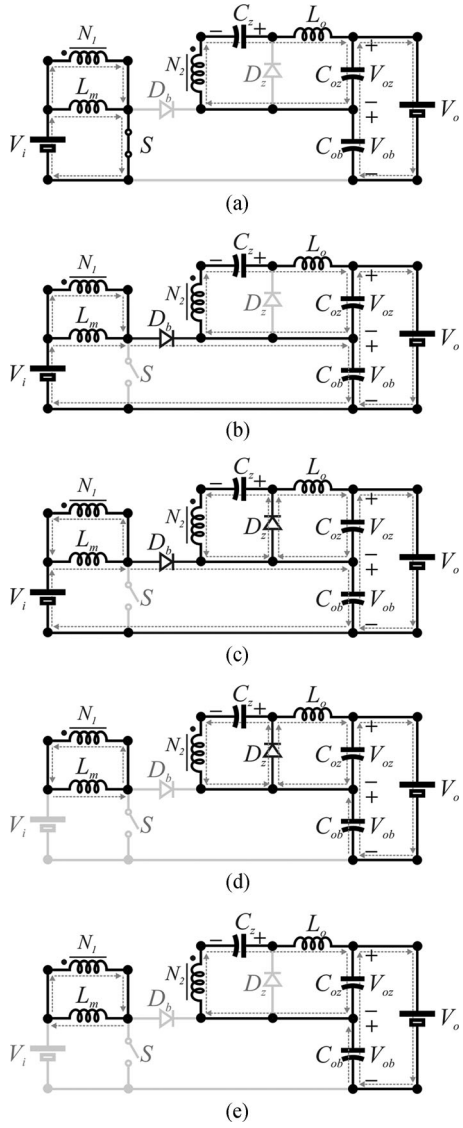

Fig. 3. Stage of operation Boost–Zeta. CCM: (a) Stage 1. (b) Stage 2. (c) Stage 3. DCM: (a) Stage 1. (b) Stage 2. (c) Stage 3. (d) Stage 4. (e) Stage 5.

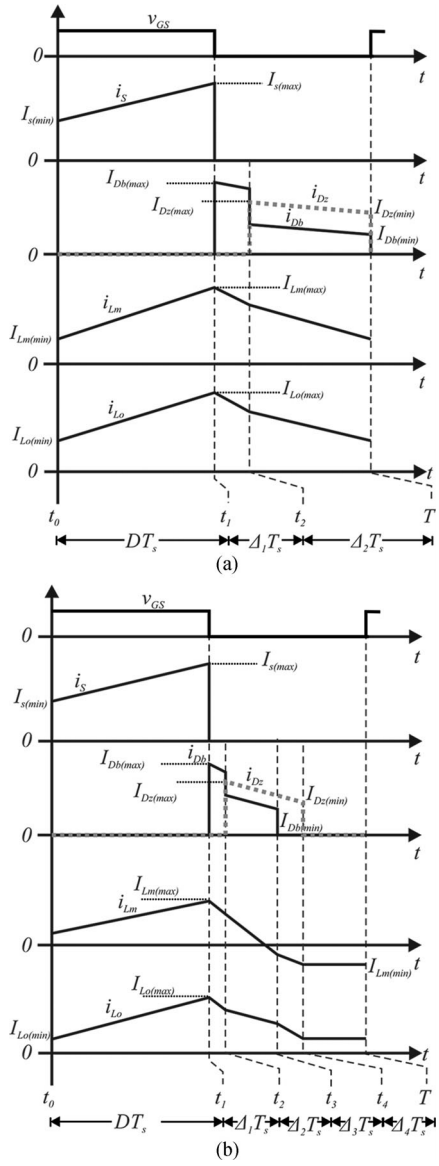

Fig. 4. Key waveforms of the proposed integrated Boost–Zeta converter. (a) CCM. (b) DCM.

$C_{\rm ob}$ and $C_{\rm oz}$ are the output capacitors of Boost and Zeta cells converters, where the output voltage of the Boost cell $(V_{\rm ob})$ and the Zeta cell $(V_{\rm oz})$ are in stacked connection thus their summed outputs voltage $(V_o = V_{\rm ob} + V_{\rm oz})$. As it can be seen the central energy storage is connected to the output of the proposed integrated Boost–Zeta converter, and the other possible DRERs are represented by a current source.

For one switching period, the operation of the converter in continuous-conduction mode (CCM) can be divided into three stages and in discontinuous-conduction mode (DCM) in five stages. The equivalent circuit for each stage in CCM is shown in Fig. 3(a)–(c) and its key waveforms are depicted in Fig. 4(a). For the DCM, the corresponding circuit for each stage is shown in Fig. 3(a)–(e) and its key waveforms are depicted in Fig. 4(b). For the description of circuit operation (and for the subsequent dc-gain derivation in the next section), the following assumptions are made:

1) the converter operates in steady state;
2) the input and output voltages are constant;
3) the relation between the primary and secondary of the coupled inductor is given by $N = \frac{N_2}{N_1}$;
4) the capacitors $C_{\rm ob}$, $C_{\rm oz}$, and C_z are large enough to assume that voltages $V_{\rm ob}$, $V_{\rm oz}$, V_o, and V_{Cz} are constant;
5) all semiconductor devices are ideal, i.e., lossless.

The operation processes are specified as follows.

Stage 1 [t_0–t_1, Fig. 3(a)]: This stage begins when S is turned ON. The diodes D_z and D_b are reverse biased with a voltage equal to $-(NV_i + V_{\rm oz})$ and $-V_{\rm ob}$, respectively. Both inductors L_m and $\rm L_o$ are magnetizing with voltage V_i and NV_i, respectively. Thus, the currents $i_{\rm Lm}$ and $i_{\rm Lo}$ increase linearly, as defined by (1) and (2), respectively. Consequently, the current through the switch S is given by the sum of the inductors current, as defined by (3). During this stage, capacitors C_z and $C_{\rm ob}$ discharge

and capacitor $C_{\rm oz}$ charges up

$$i_{\rm Lm} = \frac{V_i}{L_m}t + I_{Lm(0)} \tag{1}$$

$$i_{\rm Lo} = \frac{NV_i}{L_o}t + I_{Lo(0)} \tag{2}$$

$$i_s = i_{\rm Lm} + Ni_{\rm Lo}. \tag{3}$$

This stage lasts until the switch is turned OFF at t_1

$$DT_s = t_1 - 0. \tag{4}$$

Stage 2 [t_1–t_2, Fig. 3(b)]: At time $t = t_1$, the switch S is turned OFF and the diode D_b starts to conduct. At this stage, all characteristics related to inductors, capacitors, and diodes D_z remain equal to the previous stage. The currents $i_{\rm Lm}$ and $i_{\rm Lo}$ are defined by (5) and (6), respectively. The current through the diode D_b is equal to the primary current of the coupled inductor, given by (7). The current through the switch S is zero

$$i_{\rm Lm} = \frac{V_i - V_{\rm ob}}{L_m}t + I_{Lm(t_2)} \tag{5}$$

$$i_{\rm Lo} = -\frac{V_{\rm oz}}{L_o}t + I_{Lo(t_2)} \tag{6}$$

$$i_{\rm Db} = i_{\rm Lm} + i_{N1}. \tag{7}$$

This stage lasts until the diode D_z starts to conduct

$$\Delta_1 T_s = \frac{\left(i_{N1(t_2)} - I_{Lm(t_1)} - I_{Lo(t_2)}\right) L_o L_m}{\left(V_i - V_{\rm ob}\right)\left(N^2 L_m + L_o\right)}. \tag{8}$$

Stage 3 [t_2–t_3, Fig. 3(c)]: This stage starts when the diode D_z starts to conduct. At this stage, the voltage across inductors L_m and L_o are equal to $(V_i - V_{\rm ob})$ and $-V_{\rm oz}$, respectively. The energy stored in L_m is transferred to capacitor C_z and to the filter capacitor $C_{\rm ob}$. Similarly, the energy stored in L_o is transferred to the filter capacitor $C_{\rm oz}$. At this stage, all characteristics related to inductors, capacitors, and diodes D_b remain equal to the previous stage. Only the current in the diode D_z is changed, as shown by

$$i_{\rm Dz} = i_{\rm Lo} + i_{N2}. \tag{9}$$

In CCM operation, the diode turns off at T_s, when switch S is turned ON, starting a new switching period.

In DCM operation, the diode D_b turns off at time t_3

$$\Delta_2 T_s = (1 - (\Delta_1 + D))T_s \tag{10}$$

$$\Delta_2 T_s = \frac{\left(i_{\rm Dz} + I_{Lo(t_2)}\right) L_o}{2V_{\rm oz}}. \tag{11}$$

Stage 4 [t_3–t_4, Fig. 3(d)]: This stage begins when the diode D_b turns OFF. At this stage, the currents $i_{\rm Db}$ is zero, given by

$$i_{\rm Db} = 0. \tag{12}$$

This stage lasts until the diode D_z is turned off

$$\Delta_3 T_s = \frac{\left(i_{N1(t_3)} - I_{Lm(t_3)} - I_{Lo(t_3)}\right) L_o L_m}{\left(V_i - V_{\rm ob}\right)\left(N^2 L_m + L_o\right)}. \tag{13}$$

Stage 5 [t_4–T_s, Fig. 3(e)]: At $t = t_4$, all semiconductors are turned OFF, i.e., switch S and diodes D_b and D_z, are turned OFF. At this stage, the currents $i_{\rm Db}$ and $i_{\rm Dz}$ are zero (14). The currents $i_{\rm Lo}$ and $i_{\rm Lm}$ are equal in modulus, and have opposite direction, as defined in (15). Depending on the ratio L_m/L_o and I_i/I_o, two cases can occur:

1) First case: $I_{\rm Lm(0)} > 0$ and $I_{\rm Lo(0)} < 0$;
2) Second case: $I_{\rm Lm(0)} < 0$ and $I_{\rm Lo(0)} > 0$;

$$i_{\rm Db} = i_{\rm Dz} = 0 \tag{14}$$

$$i_{\rm Lo} = -i_{\rm Lm}. \tag{15}$$

This stage lasts until the switch is turned on

$$\Delta_4 T_s = (1 - (\Delta_4 + \Delta_3 + \Delta_2 + D))T_s. \tag{16}$$

IV. Steady-State Analysis

This section presents the steady-state analysis of the proposed integrated Boost–Zeta converter for CCM, DCM, and boundary-conduction mode (BCM).

A. CCM Operation

By applying the voltage–second balance principle on L_m and L_o, the voltage across the capacitor $C_{\rm ob}$ and $C_{\rm oz}$ can be represented by

$$\int_0^{T_s} v_{\rm Lm} + \int_0^{T_s} v_{\rm Lo} = 0. \tag{17}$$

So, the static voltage gain in CCM can be found

$$M_{\rm CCM} = \frac{V_o}{V_i} = \frac{ND + 1}{1 - D} - \frac{f_s L_k}{(1 - D)\, V_i} \tag{18}$$

which is the sum of the static gain of the boost cell (19) and the isolated Zeta cell (20) and leakage inductance of the coupled inductor may affect (21):

$$\frac{V_{\rm ob}}{V_i} = \frac{1}{1 - D} \tag{19}$$

$$\frac{V_{\rm oz}}{V_i} = \frac{ND}{1 - D} \tag{20}$$

$$V_{LK} = \frac{f_s L_k}{(1 - D)\, V_i} \tag{21}$$

where $f_{\rm s}$ is the switching frequency and L_k is the leakage inductance of the coupled inductor.

Fig. 5(a) depicted the voltage gain for the proposed converter versus the duty ratio under various leakage inductance (L_k) coefficients of the coupled inductor. It is seen that the voltage gain is not very sensitive to the leakage inductance coefficient. It is necessary to increase the value of leakage inductance coefficients, so it is possible to see their effect on the voltage gain. In other hand, when $L_{\rm k}$ is equal to 0, the ideal voltage gain is written as

$$M_{\rm CCM} = \frac{V_o}{V_i} = \frac{ND + 1}{1 - D}. \tag{22}$$

In order to simplify the following analysis, the leakage of the coupled inductor is considered zero $(L_k = 0\,{\rm H})$.

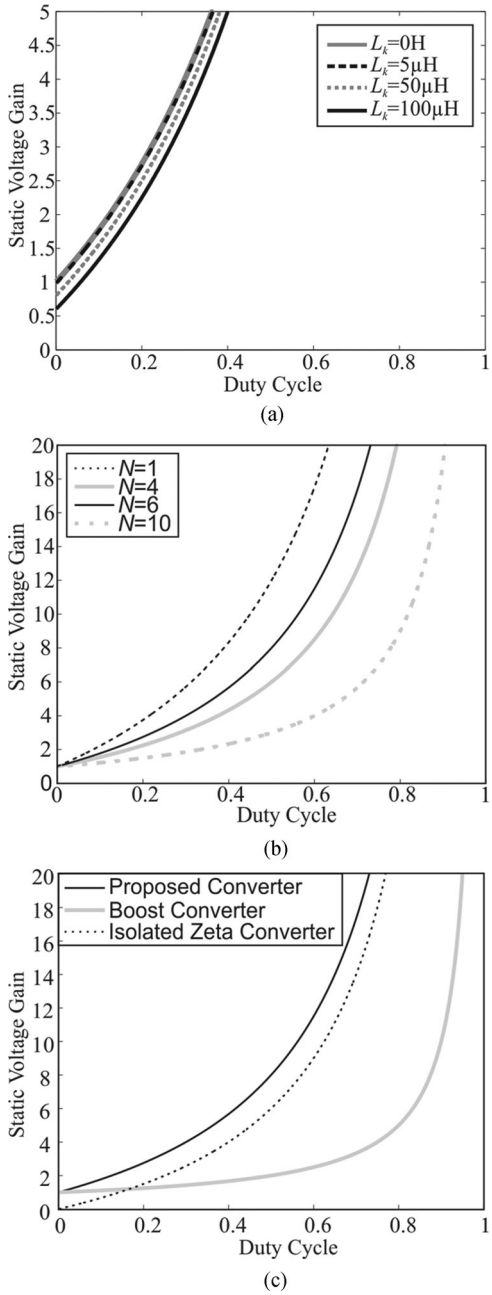

Fig. 5. Static voltage gain versus duty ratio: (a) of the proposed converter with different value for the leakage inductance (L_k) of the coupled inductor. with ($N = 6$); (b) of the proposed converter with different turns ratio (N) of the coupled inductor; and (c) of the proposed converter with Boost converter and isolated Zeta converter with $N = 6$.

The schematic of the voltage gain for the proposed converter versus the duty ratio under various turns ratio coefficients coupled inductor is shown in Fig. 5(b). It is seen that the voltage gain is very sensitive to the turn's ratio coefficient. Fig. 5(c) shows the voltage gain versus the duty ratio of the proposed converter as compared to the standard boost converters and the isolated Zeta converter, with $N = 6$. It is possible to observe that the voltage gain of the proposed converter is higher than those of the converters Boost and isolated Zeta.

B. DCM Operation

The DCM operation has five stages, previously discussed. By applying the voltage–second balance principle on L_m and L_o, the voltage across the capacitor $C_{\rm ob}$ and $C_{\rm oz}$ can be represented by (17). For the normalized input current, due the PV, the static gain for the DCM operation is given by

$$M_{\rm DCM} = \frac{V_o}{V_i} = \frac{(N+1)\,D^3}{I_{\rm inor} - D^3} + 1. \tag{23}$$

On other hand, for the normalized output current, due the charge of the CESD, the static gain for the DCM operation is given by

$$M_{\rm DCM} = \frac{2(ND+1)^2}{-(ND+1)^2 \pm \sqrt{\left((ND+1)^2+4\right)(ND+1)^2 + I_{\rm onor}}}. \tag{24}$$

C. BCM Operation

If the proposed converter is operated in BCM, the voltage gain of CCM operation is equal to the voltage gain of the DCM operation. For the normalized input current, the static gain for BCM is given by (25) and for the normalized output current (26):

$$M_{\rm BCM} = \frac{V_o}{V_i} = \frac{N\sqrt{I_{\rm inor}} + 1}{1 - \sqrt{I_{\rm inor}}} \tag{25}$$

$$M_{\rm BCM} = \frac{V_o}{V_i} = \frac{N\,(1 - I_{\rm onor}) + 1}{I_{\rm onor}}. \tag{26}$$

Using (22), (23), and (25), Fig. 6(a) shows the curve of $I_{\rm inor}$ versus the static gain. Because the source is a PV panel, Fig. 6(a) depicted the behavior of the normalized input current versus static gain, considering a constant input voltage. So, by (22), (24), and (26), Fig. 7(b) shows the curve of $I_{\rm onor}$ versus the static gain. Due to the CESD, Fig. 6(b) depicted the behavior of the normalized output current versus static gain, considering a constant output voltage.

V. Comparative Analysis

This section presents a comparative analysis of the proposed converter to the Boost and isolated Zeta converters, evaluating the voltage stress in semiconductors. To simplify this analysis, the converters are in CCM operation.

Table I summarizes the voltage gain and normalized voltage stress of key components of active as well as passive switches for the proposed converter, Boost converter, and isolated Zeta converter.

For comparison, the voltage gains, switch stresses, and diodes stresses of the converters. It is seen from Table I that a much higher static gain can be achieved and the voltage stress on semiconductors of the proposed Boost–Zeta converter is smaller than others converter. As a result, one can expect that with proper design, the proposed converter can adopt switch components with lower voltage ratings to achieve higher efficiency.

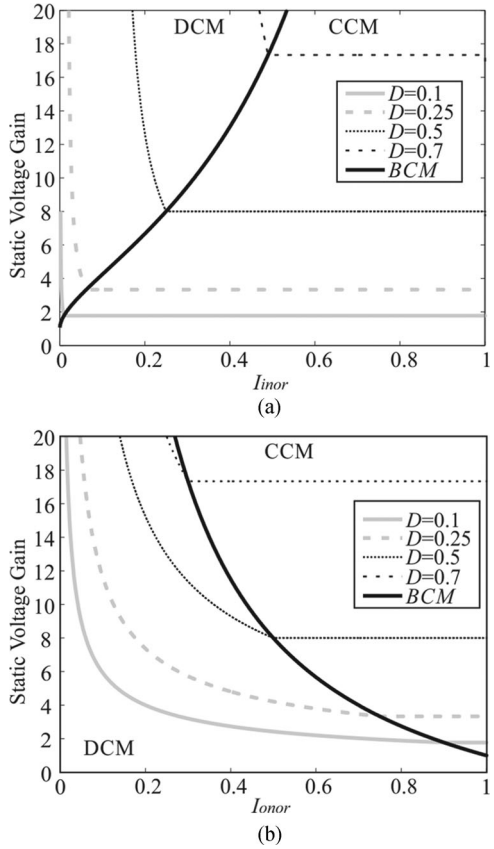

Fig. 6. Boundary condition of the proposed converter for (a) I_{inor} versus static voltage gain, $N = 6$ and (b) I_{onor} versus static voltage gain, $N = 6$.

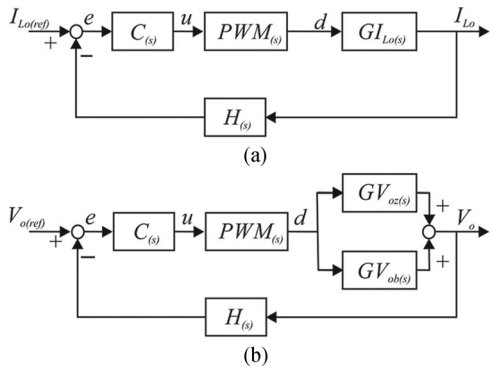

Fig. 7. Block diagrams for the system. (a) Current closed loop and (b) voltage closed loop.

VI. Modeling and Control of the Proposed Integrated Boost–Zeta Converter

This section presents an alternative way to model the integrated Boost–Zeta converters.

A. Proposed Concept of Disaggregation

In order to prevent a complex small-signal model, which is not straightforward process, because the integrated Boost–Zeta converter is connected in stacked structure and is a fifth-order model, the following assumptions are made.

TABLE I
Performance Comparison

Converters		Boost	Isolated Zeta	Integrated Boost–Zeta
Voltage Gain	M_{CCM}	$\frac{1}{1-D}$	$\frac{ND}{1-D}$	$\frac{ND+1}{1-D}$
Switch S	$\frac{V_s}{V_i}$	$\frac{1}{1-D}$	$\frac{D}{1-D}+1$	$\frac{1}{1-D}$
Diode D_{b}	$\frac{V_{\mathrm{Db}}}{V_i}$	$\frac{1}{1-D}$	–	$\frac{1}{1-D}$
Diode D_{z}	$\frac{V_{\mathrm{Dz}}}{V_i}$	–	$\frac{N}{1-D}$	$\frac{N}{1-D}$

1) To avoid complex interaction between the Boost and Zeta converter operation, first, the integrated converter is separated into each converter: the boost and Zeta converter.
2) Both Boost and Zeta converter operate with the same duty cycle and independently.
3) Output current of the converter $(I_o = I_{\mathrm{bat}})$ is the average current of the inductor $L_o\,(i_{\mathrm{Lo}})$; therefore, to find the model of the i_{Lo} and control this current, is considered only for the Zeta converter [see Fig. 7(a)].
4) There is no interference between the output voltages of each stacked output (V_{ob} and V_{oz}). This feature is fundamental to propose that the integrated converter can be modeled by means of the sum of each former converter as illustrated in the diagrams of Fig. 7(b).

In the following section, the small-signal models for the output current and output voltage are derived. Since the disaggregation is true, the modeling process makes use of standard state-space averaging approach for Boost and Zeta converters presented in [22]–[25].

B. Small-Signal Modeling for Output Current to Duty-Cycle Transfer Function

Averaged models of the separated converter can be easily derived by using an averaged PWM switch model for CCM or for DCM. Linearization of the low-frequency averaged model is derived using the state variables. The small-signal linear models can be derived substituting the perturbation matrices into the average models.

To find the output current to duty-cycle transfer function, it is required only to define the current through inductor L_{o}. This way

$$Gi_{\mathrm{Lo}}(s) = \frac{i_{\mathrm{Lo}}}{d}(s) = \frac{p_3 s^3 + p_2 s^2 + p_1 s + p_0}{q_4 s^4 + q_3 s^3 + q_2 s^2 + q_1 s + q_0} \quad (27)$$

where the coefficients are shown in the Appendix.

C. Small-Signal Modeling for Output Voltage to Duty-Cycle Transfer Function

In the same way, to find the output voltage to duty-cycle transfer function, a similar approach to the previous sections

TABLE II
PARAMETERS OF INTEGRATED BOOST–ZETA CONVERTER

Symbol	Parameters Calculate	Prototype
N	6	6
L_m	95.2 μH	95.2 μH
L_o	10.12 mH	10.12 mH
C_z	902.02 nF	1 μF
$C_{\rm oz}$	45.1 nF	68 nF
$C_{\rm ob}$	4 μF	3.3 μF
f_s	100 kHz	100 kHz
MOSFET S	60 V/8 A	IRFP150A (100 V/42 A)
D_z	360 V/0.7 A	MBR40250G (250 V/40 A)
D_b	60 V/8 A	MBR20200CT (200 V/20 A)

is carried out. Nevertheless, since the output voltages of each former converter are summed of $V_{\rm ob}$ and $V_{\rm oz}$, the output voltage transfer to duty-cycle transfer function is the sum of the output voltage transfer function of both Boost (28) and Zeta (29) converters, which are given as

$$Gv_{\rm ob}(s) = \frac{v_{\rm ob}}{d}(s) = \frac{p_1 s + p_0}{q_2 s^2 + q_1 s + q_0} \tag{28}$$

$$Gv_{\rm oz}(s) = \frac{v_{\rm oz}}{d}(s) = \frac{p_3 s^3 + p_2 s^2 + p_1 s + p_0}{q_4 s^4 + q_3 s^3 + q_2 s^2 + q_1 s + q_0} \tag{29}$$

where the coefficients are shown in the Appendix.

D. Controller Design

By means of the parameters given in Table II, it is possible to design the compensators for the closed-loop system. Fig. 7(a) shows the block diagram for the closed-loop of the output current, and Fig. 7(b) shows the closed loop of the output voltage. As it can be seen, the compensators used are proportional integrator (PI), allowing the elimination of a steady-state error. The controller design procedure consists of allocating the poles in order to eliminate the steady-state error and to get maximum attenuation of the resonance, and placing the zeros to damp the overshoot and at the resonant frequency to avoid conditional stability. Finally, it is required to set the loop gain crossover frequency below a switching frequency, typically one decade less than a switching frequency.

The implementation of the compensators for output current is performed by

$$Ci_{\rm Lo} = K_i \frac{\omega_{\rm zci}}{s} \tag{30}$$

where $K_i = 108.32$ m; $\omega_{\rm zci} = 6.28$e4 rad/s. The crossover frequency obtained from the charging current control loop is 1.2 kHz and a phase margin near to 60° provides good response. Fig. 8(a) shows the bode diagram of the current $i_{\rm Lo}$ with compensator.

The implementation of the compensators for output voltage is executed by

$$Cv_o = K_v \frac{s + \omega_{zcv}}{s} \tag{31}$$

where $K_v = 385.91\,\mu$ and $\omega_{zcv} = 8.17$e3 rad/s. The cross over frequency obtained from the charging voltage control loop

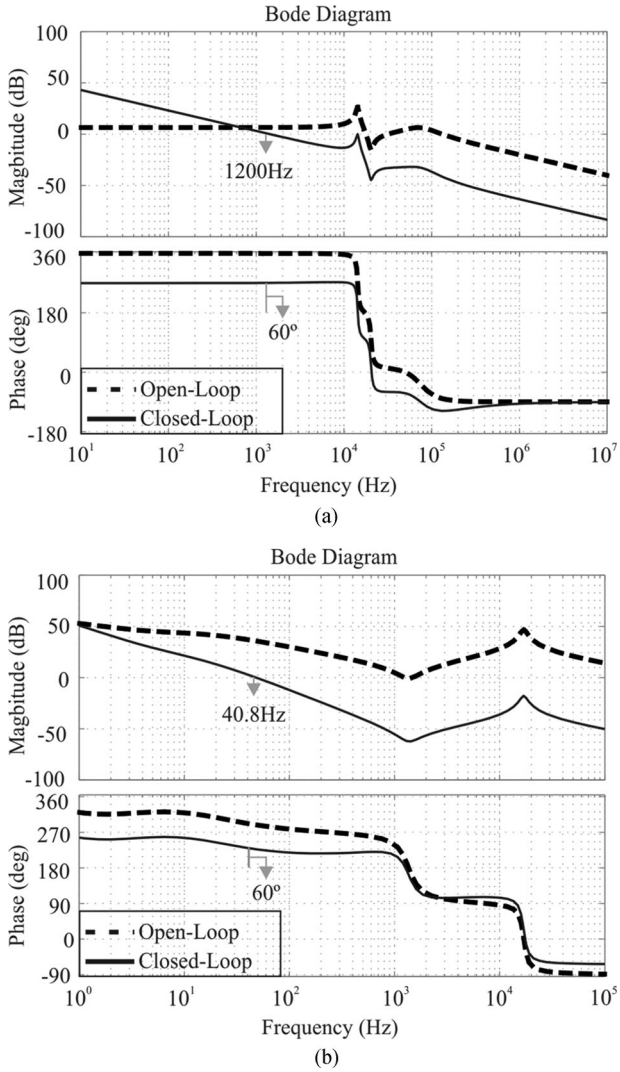

Fig. 8. Bode diagram with compensator (a) output current $i_{\rm Lo}$ and (b) output voltage v_o.

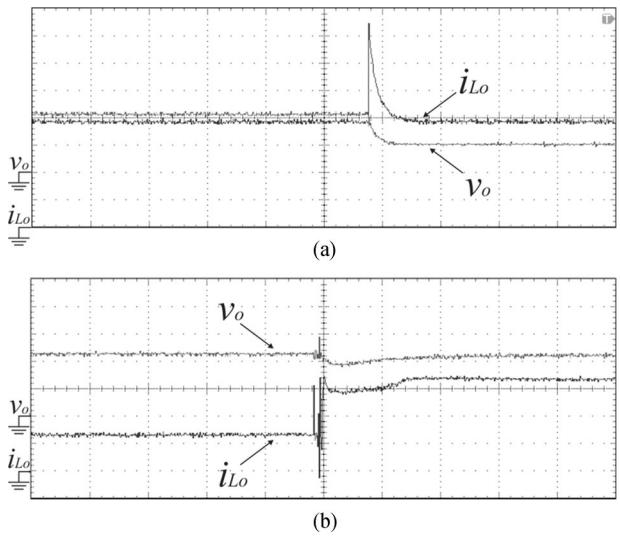

Fig. 9. Experimental results for a load step from 50% to 100%: (a) Output current $i_{\rm Lo}$ and (b) output voltage v_o.

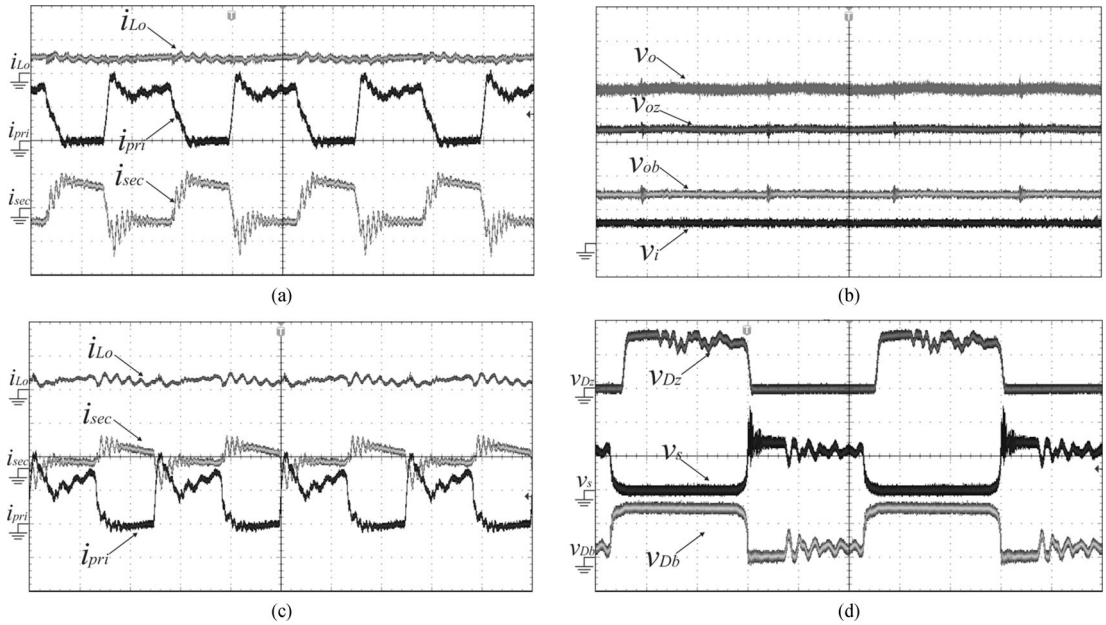

Fig. 10. Waveforms of the proposed converter prototype. (a) Currents in CCM mode. (b) Voltage in DCM mode. (c) Currents in DCM mode. (d) Voltage stress on semiconductors.

is 40.8 Hz and a phase margin near to 60° provides good response. Fig. 8(b) shows the bode diagram of the output voltage with compensator.

E. Control Validation

To validate the proposed disaggregation of modeling and control strategy of the integrated Boost–Zeta converter is validated through an experimental prototype whose main parameters are given in Table II.

Fig. 9 presents the experimental results for a load step from 50% to 100% of the output power. Fig. 9(a) shows the load step for the output current, in the CCM mode, and it is observed as a good regulation. In the DCM mode, Fig. 9(b) shows the load step for the output voltage, and it presents good performance.

These results demonstrate that the model obtained by the proposed concept disaggregation, depicted in the initial sections is adequate to design the control system for the converter, combining a well-known modeling technique with a good representation of the main dynamics of the converter.

VII. Design and Experiment of the Proposed Converter

To verify the performance of the proposed converter in the FREEDM system, a prototype circuit is implemented in the laboratory. The input data are given by the PV KYOCERA FV-250W and the central energy device storage (battery UNIPOWER GP12-7), the specifications are as follows:

1) $P_i = 250$ W, input power;
2) $V_i = 30$ V, input voltage;
3) $V_o = 240$ V, output voltage;
4) $V_{\rm ob} = 60$ V, output voltage of a Boost cell converter;
5) $V_{\rm oz} = 180$ V, output voltage of a Zeta cell converter;
6) $I_o = 0.7$ A, charging current;
7) $D = 0.5$, duty cycle;
8) $f_s = 100$ kHz, switching frequency.

The Boost–Zeta converter parameters are summarized in Table II.

The main waveforms for the Boost–Zeta converter were obtained in the laboratory and are shown in Fig. 10.

In a CCM mode, Fig. 10(a) presents the inductor L_o current $(i_{\rm Lo})$, the current in the primary of the coupled inductor $(i_{pri} = i_{\rm Lm} + i_{N1})$, and the current in the secondary of the coupled inductor $(i_{\rm sec})$.

In a DCM mode, Fig. 10(b) shows the output voltage $(V_o = 240\,{\rm V})$, the output voltage of the isolated Zeta cell $(V_{\rm oz} = 180\,{\rm V})$, the output voltage of the Boost cell $(V_{\rm ob} = 60\,{\rm V})$, and the input voltage $(V_i = 30\,{\rm V})$. Fig. 10(c) shows the inductor L_o current $(i_{\rm Lo})$, the current in the primary of the coupled inductor $(i_{\rm pri} = i_{\rm Lm} + i_{N1})$, and the current in the secondary of the coupled inductor $(i_{\rm sec})$.

Finally, in Fig. 10(d), it can be seen the voltage stress in the switch $(V_{\rm s})$, in the diode D_b $(V_{\rm Db})$, and the diode $(V_{\rm Dz})$. Thus, validating the analysis depicted in Table I for the voltage stress in the semiconductor.

In Fig. 11, the transient waveforms of the MPPT algorithm are shown. The converter can perform the MPPT function since that the panel output power is decreased from 250 to 190 W, and the converter achieves the settling time approximately at 0.50 s.

Fig. 12 shows the variation of the charging current for approximately 180 min and it provides the charge from a discharged battery bank (189 V) to a fully charge one (240 V), where the converter is in CCM. Afterward, the CESD voltage is kept regulated at 240 V. The charging current decreases approximately to 0.07 A, where the converter is in DCM, thus completing the charging process for this battery bank (18 series-connected batteries).

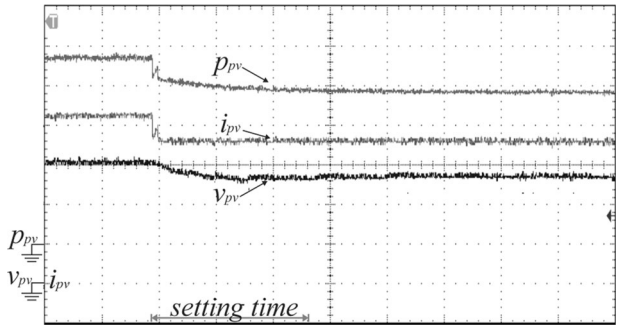

Fig. 11. Transient responses of MPPT algorithm, $p_{\rm pv}$ 50 W/div, $i_{\rm pv}$: 2 A/div, $v_{\rm pv}$: 10 V/div.

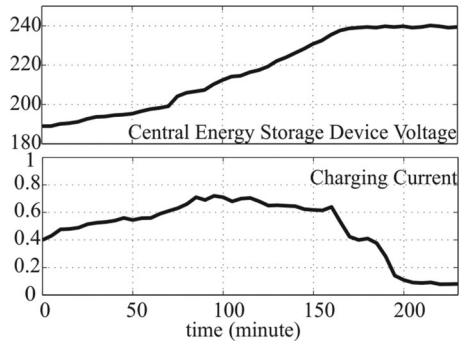

Fig. 12. Waveforms of charging CESD (batteries).

TABLE III
WEIGHTED AVERAGE EFFICIENCY OF CALIFORNIA ENERGY COMMISSION

Weighting	$P_{\rm pv}$	Average Efficiency
0.01	93.23	0.9323
0.15	93.19	13.9785
0.37	92.8	34.336
0.33	92.5	30.525
0.13	92.21	11.9873
0.01	92.16	0.9216
Total		92.6807

From the features of the PV KYOCERA FV-250W, the weighted average efficiency of California energy commission measured from the prototype is given by Table III, by using Yokogawa-WT3000E. As it can be seen, the average efficiency is 92.6807%, which is a good efficiency for a high-voltage gain converter considering the full-charge condition.

With the characteristics of PV KYOCERA FV-250W and the central energy device storage (battery UNIPOWER GP12-7), Fig. 13 shows a comparison between the proposed Boost–Zeta converter and the isolated Zeta converter prototype. As it can be seen, the proposed converter is better than isolated Zeta converter, across all ranges of the irradiation, with the maximum value 93.23% with the irradiation equal a 200 W/m². Therefore, the results show that the proposed converter has promoted the efficiency in relation to the isolated Zeta converter.

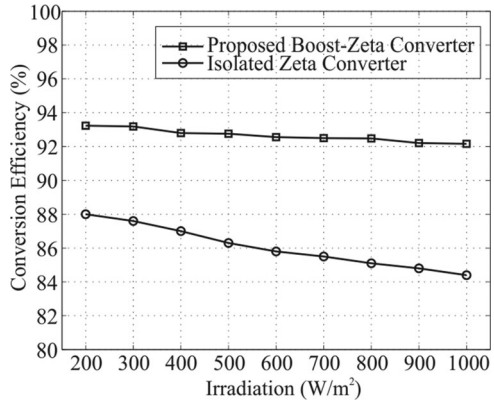

Fig. 13. Experimental conversion efficiency.

VIII. CONCLUSION

The PV converters can take advantage in FREEDM systems of reducing their complexity as well as costs to the end user. This paper presented the Boost–Zeta converters with high step-up voltage gain, supplying a 190–259 VDC of a dc bus in the proposed modified FREEDM system. The power converter is responsible for the MPPT for the PV generator and also controls the central energy device storage.

To ensure low ripple current across the central energy device storage and high-voltage gain, the Zeta cell converter has been chosen, and also, due to the fact that the current PV panel is not discontinuous and increases the voltage gain, the Boost cell converter was chosen. This combination of the cells allows achieving the qualities of each cell and also adds quality to decrease stress on the components and component values.

The converter is designed to operate in CCM and DCM modes due to central energy device storage, and it is necessary to regulate both current and voltage of the central energy device storage. The approach of the disaggregation concept for modeling and control of the proposed converter ensures good transient response when the converter is subject to load disturbances and when applied in the proposed modified FREEDM system.

Experimental results are presented and confirm the theoretical analysis.

APPENDIX

The parameters for (27) are as follows.

Parameters in polynom Q

$$q_0 = -\frac{ND(1-D)^2}{L_m L_o r_{\rm coz} N C_z C_{\rm oz}},\ q_1 = -\frac{N(1-D)^2}{NC_z L_m C_{\rm oz} R r_{\rm coz}}$$

$$q_2 = \frac{N(1-D)^2 + DL_m NC_z}{L_o r_{\rm coz} C_{\rm oz}},\ q_3 = -\frac{1}{C_{\rm oz} R r_{\rm coz}} q_4 = 1.$$

Parameters in polynom P

$$p_0 = \left(-\frac{1}{L_o r_{\rm coz}}\frac{D}{C_{\rm oz}} + \left(\frac{ND^2}{L_o} + \frac{N(1-D)^2}{L_m}\right)\right.$$

$$\times \frac{1}{NC_zC_{\rm oz}Rr_{\rm coz}}\Bigg)\frac{NV_i - V_{C_z}}{L_o}$$

$$p_1 = \frac{D^2\left(NV_{C_z}+V_i\right)}{L_oL_mC_z} + \frac{NV_i - V_{C_z}}{C_{\rm oz}Rr_{\rm coz}L_o} + \left(\frac{C_{\rm oz}Rr_{\rm coz}-1}{C_{\rm oz}Rr_{\rm coz}}\right) \times \left(\frac{Di_{\rm Lm} - DNi_{\rm Lo}}{L_oC_z}\right)$$

$$p_2 = \frac{NV_{C_z}+V_i}{C_{\rm oz}Rr_{\rm coz}L_m},$$

$$p_3 = \frac{\left(L_o+L_m\right)NV_i + V_{C_z}}{L_oL_m}.$$

The parameters for (28) are as follows.

Parameters in polynom Z

$$q_1 = \frac{1}{r_{\rm cob}C_{\rm ob}},\ q_2 = \frac{R}{{M_{\rm ob}}^2L_m}.$$

Parameters in polynom P

$$p_1 = \frac{2M_{\rm ob}-1}{RC_{\rm ob}\left(M_{\rm ob}-1\right)},\ p_2 = 2f_s\left(\frac{M_{\rm ob}-1}{DM_{\rm ob}}\right)^2.$$

Parameters for (29): Parameters in polynom Q equations are shown at the bottom of the page.

Parameters in polynom P

$$p_0 = \Bigg(\left(-\frac{N\Delta_2}{L_m}+\frac{N\Delta_4}{NL_m-L_o}\right) \times \left(-\frac{D+\Delta_2}{Lo}+\frac{\Delta_4}{\left(NL_m-L_o\right)r_{\rm coz}}\right) + \frac{\Delta_4}{N(L_m-L_o)r_{\rm coz}}\left(-\frac{D}{L_o}-\frac{\Delta_4}{NL_m-L_o}\right)\Bigg) \times \left(-\frac{D\left(D+\Delta_2\right)V_i}{2NC_zL_m}+\frac{D\left(D+\Delta_2\right)V_i}{2C_zL_o}\right)$$

$$\frac{1}{C_{\rm oz}Rr_{\rm coz}} + \frac{Rr_{\rm coz}}{\left(R+r_{\rm coz}\right)C_{\rm oz}Rr_{\rm coz}}\left(-\frac{D+ND+N\Delta_4}{NC_z}\right) \times \left(\left(-\frac{D}{L_o}-\frac{\Delta_4}{NL_m-L_o}\right)\right.$$

$$\left.\frac{\left(N^2D+1-D\right)V_i}{L_m(1-D)}+\left(-\frac{N\Delta_2}{L_m}+\frac{N\Delta_4}{NL_m-L_o}\right) \times \left(\frac{(1-2D)NV_i}{L_o(1-D)}\right)(D-R)\right)$$

$$p_1 = -\frac{DRr_{\rm coz}}{C_{\rm oz}r_{\rm coz}(R+r_{\rm coz})}\left(-\frac{D+\Delta_2}{L_o}+\frac{\Delta_4}{N(L_m-L_o)r_{\rm coz}}\right) \times \frac{\left(N^2D+1-D\right)V_i}{L_m(1-D)} - \frac{DRr_{\rm coz}}{C_{\rm oz}r_{\rm coz}\left(R+r_{\rm coz}\right)}\left(\frac{NL_m\Delta_4 - N\Delta_2\left(NL_m-L_o\right)}{NL_m-L_o}\right) \left(-\frac{D\left(D+\Delta_2\right)V_i}{2NC_zL_m}+\frac{D\left(D+\Delta_2\right)V_{in}}{2C_zL_o}\right) - \left(\frac{NL_m\Delta_4 - N\Delta_2(NL_m+NL)_o}{{NL_m}^2-L_mL_o}\right) \frac{\left(D+ND+N\Delta_4\right)(1-2D)DRr_{\rm coz}NV_i}{NC_z\left(L_o(1-D)R+r_{\rm coz}\right)} + \frac{\left(DNL_m - L_oL_o\Delta_4\right)\left(DRr_{\rm coz}(1-2D)NV\right)_i}{\left(NL_m-L_o\right)\left({L_o}^2C_{\rm oz}Rr_{\rm coz}\left(R+r_{\rm coz}\right)(1-D)\right)}$$

$$p_2 = \frac{1}{C_{\rm oz}Rr_{\rm coz}}\frac{\left(N^2D+1-D\right)V_{in}}{L_m(1-D)}\frac{(1-2D)NV_i}{L_o(1-D)} + \frac{1}{C_{\rm oz}Rr_{\rm coz}}\frac{\left(N^2D+1-D\right)V_{in}}{L_m(1-D)} \times \left(-\frac{D\left(D+\Delta_2\right)V_i}{2NC_zL_m}+\frac{D\left(D+\Delta_2\right)V_i}{2C_zL_o}\right) - \frac{1}{C_{\rm oz}Rr_{\rm coz}}\frac{\left(N^2D+1-D\right)V_i}{L_m(1-D)}\frac{(1-2D)NV_i}{L_o(1-D)} + \left(-\frac{D}{L_o}-\frac{\Delta_4}{NL_m-L_o}\right) \frac{DRr_{\rm coz}}{R+r_{\rm coz}}\frac{(1-2D)NV_i}{L_o(1-D)} + \frac{1}{C_{\rm oz}r_{\rm coz}}\frac{Rr_{\rm coz}}{R+r_{\rm coz}}\frac{(1-2D)NV_i}{L_o(1-D)}$$

$$q_0 = \frac{\left(L_m\Delta_4\left(1-N\Delta_2-1\right)\left(D+ND+1\right)\right)\left(L_o\Delta_4-\left(D+\Delta_2\right)\left(NL_m-L_o\right)r_{\rm coz}\right)}{L_o\left({NL_m}^2-L_o\right)C_zC_{\rm oz}{r_{\rm coz}}^2}$$

$$q_1 = \left(\frac{N\Delta_2}{L_m}-\frac{N\Delta_4}{NL_m-L_o}\right)\left(\frac{D+ND+N\Delta_4}{NC_z}\right)\frac{1}{C_{\rm oz}Rr_{\rm coz}}$$

$$q_2 = \left(\frac{\left(N^2\Delta_2\left(L_m-L_o\right)-NL_m\Delta_4\right)\left(D+ND+N\Delta_4\right)}{NC_z\left({NL_m}^2-L_o\right)}\right) + \left(\frac{D(NL_m-L_o)r_{\rm coz}-L_o\Delta_2\Delta_4}{(NL_m-L_o)C_{\rm oz}{r_{\rm coz}}^2}\right),\quad q_3 = -\frac{1}{C_{\rm oz}Rr_{\rm coz}},\quad q_4 = 1.$$

$$p_3 = \frac{DRr_{\mathrm{coz}}}{R + r_{\mathrm{coz}}} \left(\frac{N^2 D + 1 - D}{L_m(1-D)} V_i + \frac{1 - 2D}{L_o(1-D)} N V_i \right).$$

ACKNOWLEDGMENT

The authors are thankful for the contributions of Xilinx for material support.

REFERENCES

[1] C. M. Lai, C. T. Pan, and M. C. Cheng, "High-efficiency modular high step-up interleaved boost converter for DC-microgrid applications," *IEEE Trans. Ind. Appl.*, vol. 48, no. 1, pp. 161–171, Jan./Feb. 2012.

[2] P. Xuewei, A. K. Rathore, and U. R. Prasanna, "Novel soft-switching snubberless naturally clamped current-fed full-bridge front-end-converter-based bidirectional inverter for renewables, microgrid, and UPS applications," *IEEE Trans. Ind. Appl.*, vol. 50, no. 6, pp. 4132–4141, Nov./Dec. 2014.

[3] M. Farhadi and O. A. Mohammed, "Real-time operation and harmonic analysis of isolated and non-isolated hybrid DC microgrid," *IEEE Trans. Ind. Appl.*, vol. 50, no. 4, pp. 2900–2909, Jul./Aug. 2014.

[4] M. Farhadi and O. A. Mohammed, "Performance enhancement of actively controlled hybrid DC microgrid incorporating pulsed load," *IEEE Trans. Ind. Appl.*, vol. 51, no. 5, pp. 3570–3578, Sep./Oct. 2015.

[5] R. Ahmadi and M. Ferdowsi, "Improving the performance of a line regulating converter in a converter-dominated DC microgrid system," *IEEE Trans. Smart Grid*, vol. 5, no. 5, pp. 2553–2563, Sep. 2014.

[6] Z. Liang, R. Guo, J. Li, and A. Q. Huang, "A high-efficiency PV module-integrated DC/DC converter for PV energy harvest in FREEDM systems," *IEEE Trans Power Electr.*, vol. 26, no. 3, pp. 897–909, Mar. 2011.

[7] A. Q. Huang, M. L. Crow, G. T. Heydt, J. P. Zheng, and S. J. Dale, "The future renewable electric energy delivery and management (FREEDM) system: The energy internet," *Proc. IEEE*, vol. 99, no. 1, pp. 133–148, Jan. 2011.

[8] F. Xue, Y. Zhao, R. Yu, W. Yu, and A. Q. Huang, "Stationary energy storage system based on modular high voltage battery modules," in *Proc. IEEE First Int. Conf. DC Microgrids*, Jun. 2015, pp. 7–10.

[9] A. Q. Huang, "Renewable energy system research and education at the NSF FREEDM systems center," in *Proc. IEEE Power Energy Soc. Gen. Meet.*, Jul. 26–30, 2009, pp. 1–6.

[10] A. Q. Huang, "FREEDM system—A vision for the future grid," in *Proc. IEEE in Power Energy Soc. Gen. Meet.*, Jul. 25—29, 2010, pp. 1–4.

[11] O. Khan, W. Xiao, and H. H. Zeineldin, "Gallium-nitride-based submodule integrated converters for high-efficiency distributed maximum power point tracking PV applications," *IEEE Trans. Ind. Electron.*, vol. 63, no. 2, pp. 966–975, Feb. 2016.

[12] D. Bol, E. H. Boufouss, D. Flandre, and J. De Vos, "A 0.48 mm^2 5 μW-10 mW indoor/outdoor PV energy-harvesting management unit in a 65 nm SoC based on a single bidirectional multi-gain/multi-mode switched-cap converter with supercap storage," in *Proc. Eur. Solid-State Circuits Conf.*, Sep. 14–18, 2015, pp. 241–244.

[13] I. Laird and D. D. C. Lu, "High step-up DC/DC topology and MPPT algorithm for use with a thermoelectric generator," *IEEE Trans. Power Electron.*, vol. 28, no. 7, pp. 3147–3157, Jul. 2013.

[14] N. Katayama, S. Tosaka, T. Yamanaka, M. Hayase, K. Dowaki, and S. Kogoshi, "New topology for DC–DC converters used in fuel cell–electric double layer capacitor hybrid power source systems for mobile devices," *IEEE Trans. Ind. Appl.*, vol. 52, no. 1, pp. 313–321, Jan./Feb. 2016.

[15] K. E. Holbert, L. L. Grable, A. Overbay, and B. J. O. Nzekwe, "FREEDM precollege programs: Inspiring generation Y to pursue careers in the electric power industry," *IEEE Trans. Power Syst.*, vol. 29, no. 4, pp. 1888–1896, Jul. 2014.

[16] P. Tatcho, H. Li, Y. Jiang, and L. Qi, "A novel hierarchical section protection based on the solid state transformer for the future renewable electric energy delivery and management (FREEDM) system," *IEEE Trans. Smart Grid*, vol. 4, no. 2, pp. 1096–1105, Jun. 2013.

[17] P. J. Cheng, C. H. Cheng, and S. B. Hong, "Optimal battery chargers for photovoltaic system based on fuzzy theory and Taguchi method," in *Proc. Int. Conf. Adv. Robot. Intell. Syst.*, Tainan, 2013.

[18] J. Fattal and P. B. D. N. Karami, "Review on different charging techniques of a lithium polymer battery," in *Proc. Int. Conf. Technol. Adv. Electr., Electron. Comput. Eng.*, Apr. 29, 2015–May 1, 2015, pp. 33–38.

[19] A. M. S. S. Andrade, J. R. Dreher, and M. L. S. Martins, "High step-up integrated DC-DC converters: Methodology of synthesis and analysis," in *Proc. Brazilian Power Electron. Conf.*, Oct. 27–31, 2013, pp. 50–57.

[20] A. M. S. S. Andrade, J. C. Giacomini, C. Rech, L. Schuch, and M. L. D. S. Martins, "Boost-Zeta high step-up PV module integrated converter," in *Proc. IEEE Energy Convers. Congr. Expo*, Montreal, QC, Canada, 2015, pp. 1046–1053.

[21] A. M. S. S. Andrade, R. C. Beltrame, L. Schuch, and M. L. D. S. Martins, "PV module-integrated single-switch DC/DC converter for PV energy harvest with battery charge capability," in *Proc. 11th IEEE/IAS Int. Conf. Ind. Appl.*, Juiz de Fora, Brazil, 2014, pp. 1–8.

[22] R. W. Erickson and D. Maksimovic, *Fundamentals of Power Electronics*, 2nd ed. New York, NY, USA: Springer, 2001.

[23] V. Eng, U. Pinsopon, and C. Bunlaksananusorn, "Modeling of a SEPIC converter operating in continuous conduction mode," in *Proc. 6th Int. Conf. Electr. Eng./Electron., Comput., Telecommun. Inf. Technol.*, May 6—9, 2009, vol. 1, pp. 136–139.

[24] V. Eng and C. Bunlaksananusorn, "Modeling of a SEPIC converter operating in discontinuous conduction mode," in *Proc. 6th Int. Conf. Electr. Eng./Electron., Comput., Telecommun. Inf. Technol.*, May 6–9, 2009, vol. 1, pp. 140–143.

[25] A. M. S. S. Andrade, L. Schuch, and M. L. D. S. Martins, "Modeling and control of high step-up integrated converters," in *Proc. 2015 IEEE 24th Int. Symp. Ind. Electron.*, Buzios, Brazil, 2015, pp. 325–330.

António Manuel Santos Spencer Andrade (S'15) was born in Ribeira Grande, Cabo Verde, in 1989. He received the Bachelor of Science degree in automation and control engineering from the University of Caxias do Sul, Caxias do Sul, Brazil, in 2012, and the M.S. degree in electrical engineering from the Federal University of Santa Maria, Santa Maria, Brazil, in 2015, where he is currently working toward the Ph.D. degree in electrical engineering.

His research interests include renewable energy, dc–dc converters, microinverters.

Mr. Andrade is a Member of the Brazilian Power Electronics Society (SOBRAEP) and several IEEE Societies.

Luciano Schuch (S'03–M'06) was born in Santa Maria, Brazil, in 1974. He received the B.S., M.S., and the Ph.D. degrees in electrical engineering (subarea power electronics) from the Federal University of Santa Maria (UFSM), Santa Maria, Brazil, in 1999, 2001, and 2007, respectively.

Since 2009, he has been with the Power Electronics and Control Research Group (GEPOC), UFSM, where he is currently a Professor. His research interests include PV systems, UPS, and high-performance power converters.

Mario Lúcio da Silva Martins (M'10) was born in Palmeira das Missoes, RS, Brazil, in 1976. He received the B.S., M.S., and Ph.D. degrees in electrical engineering from the Federal University of Santa Maria, Santa Maria, Brazil, 1999, 2002, and 2008, respectively.

From 2006 to 2012, he was with the Federal University of Technology-Parana, Pato Branco, Brazil. In 2012, he joined the Department of Electronics and Computation, Federal University of Santa Maria. His research interests include high-performance power converters, uninterruptible power supplies, and power converters for renewable energy.

Dr. Martins is a Member of the Brazilian Power Electronics Society (SOBRAEP) and several IEEE Societies.